Focused 70-cm Wavelength Radar Mapping of the Moon

Journal:	*Transactions on Geoscience and Remote Sensing*
Manuscript ID:	draft
Manuscript Type:	Regular paper
Date Submitted by the Author:	n/a
Complete List of Authors:	Campbell, Bruce; Smithsonian Institution, Center for Earth & Planetary Studies Campbell, Donald; Cornell, Astronomy Margot, Jean Luc; Cornell, Astronomy Ghent, Rebecca; University of Toronto, Geology Nolan, Michael; Arecibo, Radar Astronomy Chandler, John; Smithsonian, Astrophysics Carter, Lynn; Smithsonian, CEPS Stacy, Nicholas; DSTO, Radar
Keywords:	Moon, Radar imaging

Focused 70-cm Wavelength Radar Mapping of the Moon

Bruce A. Campbell
Center for Earth and Planetary Studies
Smithsonian Institution
MRC 315
PO Box 37012
Washington, DC 20013-7012
Phone: (202) 633-2472
Fax: (202) 786-2566
campbellb@si.edu

Donald B. Campbell and J.L. Margot
Department of Astronomy
Cornell University
Ithaca, NY 14853

Rebecca R. Ghent
Department of Geology
University of Toronto
22 Russell Street
Toronto, ON M5S3B1 Canada

Michael Nolan
Arecibo Observatory
HCO3 Box 53995
Arecibo, PR 00612

John Chandler
Smithsonian Astrophysical Observatory
60 Garden Street
Cambridge, MA 02138

Lynn M. Carter
Center for Earth and Planetary Studies
Smithsonian Institution
MRC 315
PO Box 37012
Washington, DC 20013-7012

Nicholas J.S. Stacy
Defence Science and Technology Organization
Box 1500
Edinburgh, SA 5111
Australia

Submitted to IEEE Transactions on Geoscience and Remote Sensing

December 2006

Abstract. We describe new 70 cm wavelength radar images of the lunar near side and limb regions obtained via a SAR patch-focusing reduction technique. The data were obtained by transmitting a circularly polarized simple pulsed waveform from the 305 m Arecibo telescope in Puerto Rico and receiving the echo in both senses of circular polarization with the Robert C. Byrd Green Bank Telescope in West Virginia. The resultant images in both polarizations have a spatial resolution as fine as 320 m x 450 m at the limbs of the Moon. The patch-focusing technique is a computationally efficient method for compensating for range migration and Doppler (azimuth) smearing over the long coherence times, ~1000 secs, needed to achieve the required Doppler resolution. 3-9 looks are averaged for speckle reduction and to improve the signal-to-noise ratio. At this long wavelength, the radar signal penetrates up to several tens of meters into the dry lunar surface materials, revealing details of the bulk loss properties and decimeter-scale rock abundance not evident in multi-spectral and other remote sensing data. We present an application of the new radar data to compositional and relative age studies of basalt flow complexes in Mare Serenitatis. These results suggest that high-resolution, long-wavelength radar data can be an important factor in differentiating basalt flow age differences, particularly for smaller deposits that may not have robust crater statistics. The new 70-cm lunar radar data are being archived in the NASA Planetary Data System.

Index Terms: Moon, radar imaging

I. Introduction

Earth-based remote sensing studies of the Moon include observations of UV, visible, and IR reflectance, thermal infrared properties during eclipse, and scattering or emission in the microwave region. Radar studies are of particular interest as the only method for probing to depths beyond a few cm (the range of thermal infrared variations), and for their sensitivity to the bulk geochemical properties and rock abundance of the lunar regolith. Synoptic datasets for the Moon, covering most of the visible near side, have been collected at 3.8 cm (2-4 km resolution) [1], 70-cm (4-8 km resolution) [2], and 7.5-m wavelengths (10-30 km resolution) [3]. Selected areas have been mapped at spatial resolutions of 20-150 m using 3.0-cm [4, 5, 6] and 12.6-cm wavelengths [7, 8, 9].

70-cm wavelength radar data have proven particularly useful in probing the upper several meters of the regolith. Backscatter variations at this wavelength are correlated with the local and regional geologic properties, such as varying titanium content in mare basalts [10, 11], block-size distribution in ejecta from large craters and impact basins [12, 13], changes in bulk regolith loss tangent due to buried ancient mare basalt units [14] and rock-poor regional pyroclastic deposits formed by volcanic fire fountains [15, 16, 17]. Based on this experience, there are strong reasons to extend geologic studies to finer spatial resolution and to extend the coverage over areas near the poles and limbs that have not been investigated previously. To this end, we have been collecting data for a new radar backscatter map of the Moon's near side with horizontal spatial resolutions of 450-900 m.

The next three sections of this paper discuss the radar mapping and calibration methodology while the last section describes how radar echo information complements

the estimation of mare basalt titanium content and age from multi-spectral and photographic data.

Because of the large distances and relatively low resolution, imaging of planetary bodies using Earth based radars normally only requires unfocused processing of the data, usually referred to in the field of planetary radar astronomy as delay-Doppler mapping [18]. However, the ~9 arcmin beamwidth of the Arecibo antenna is ~30% of the angular diameter of the Moon so that a single observation images a very large field of view on the lunar surface. At the desired resolution of a few hundred meters there is significant range migration and Doppler smearing at the edges of the field of view requiring a focused reduction of the data. To minimize the computational effort, a simple "patch" focusing scheme [7] was implemented in which an unfocused delay-Doppler analysis followed by a coordinate transformation into selenographic coordinates are used to image a "patch" centered on a target location, the geographic point on the Moon for which the changing range and range rate are compensated over the integration period (16 minutes). The patch size is dictated by the size of the area over which the unfocused processing does not result in smearing of more than 0.5 of a pixel due to range migration and Doppler drift. A new target location is then chosen and its computed range and phase history, relative to the initial target location, is used to "move" the data to this location and another delay-Doppler analysis performed to obtain an image over the "patch". This process is repeated until the entire field of view is imaged.

II. Data Collection

We transmit a left-circularly polarized radar signal at 430 MHz (radar wavelength, λ, of 0.7 m) from the 305-m National Science Foundation's (NSF's) Arecibo Telescope in Puerto Rico. The transmitted wave form is a 3-μs long pulse at a pulse repetition period (PRP) of 15 ms, yielding a range resolution, Δr, of 450 m. The pulse repetition frequency (PRF) and its inverse, the PRP, must satisfy two conditions: (1) sample the frequency-broadened echo from the Moon at the relevant Nyquist frequency, and (2) not exceed the delay depth of the Moon to avoid time ambiguity between successive pulses. The round-trip-time delay depth of the Moon (radius 1738 km) is 11.59 ms, while the maximum apparent limb-to-limb bandwidth at 430 MHz is ~12 Hz. A PRF of ~67 Hz (15 ms PRP) easily satisfies the ambiguity constraints, and samples a region "off the Moon" for system noise power measurements.

The reflected echoes in both circular polarizations are received at the 100-m NSF Robert C. Byrd Green Bank Telescope (GBT) in West Virginia, quadrature mixed to baseband (there are several mixing and filtering stages) and the resultant complex voltages sampled at a 1 MHz rate [19] (Figure 1). The GBT is used as the receiving station because the Arecibo 430-MHz mono-static radar system cannot receive the echo in both senses of circular polarization for nearby solar system targets such as the Moon, which has a round-trip-light time of ~2.5 sec. Echoes polarized in the same sense as that transmitted are termed "SC", and often referred to as "depolarized" since they arise from effects such as multiple scattering or scattering from sharp edges. Echoes in the opposite sense to that transmitted, the one expected for a mirror-like reflection, are termed "OC" or "polarized".

The GBT is not equipped to compensate in real time for changes in the range and range-rate (Doppler shift) to the target location, normally the beam center on the Moon, so these operations are performed on the transmitted signal at Arecibo. The echo from the target location arrives at the GBT at exactly 430.0 MHz and with a PRP of 15.0 ms. The range and range-rate corrections are applied by simply Doppler shifting the transmitted signal and the 20 MHz clock to the timing generator. New values are applied at 1.0 ms intervals based on ephemeredes generated at the Smithsonian Astrophysical Observatory that predict the range and Doppler shift to the target location, plus the pointing information for the antennas, at 1 minute intervals. A 7^{th} order polynomial is fitted to the Doppler shift values spanning the anticipated observation time and evaluated for each moment that the Doppler shifts are updated. A frequency offset of a few Hz, f_o, is added to the incoming signal at the GBT to move the center frequency of the lunar echoes away from zero Hz to avoid problems related to DC level errors. During data acquisition, each quadrature channel is digitized using 4-bit analog-to-digital (A/D) conversion and the resultant data stream stored on disk. The initial data analysis converts the 4-bit samples to floating-point values and sums the 1-μs spaced samples in pairs yielding 7500 2-μs "range bins" per PRP. This retains a 50% over-sampling of the 3 μs pulse. We further sum coherently groups of four individual PRPs, yielding an effective PRP of 60 ms (PRF of ~17 Hz). Each radar coherence interval, T_{coh}, or "look", is 983 s long (65536 PRPs), giving a frequency resolution of ~1 mHz. Since the maximum limb-to-limb bandwidth of the Moon is ~12 Hz, there is a comfortable margin to avoid frequency aliasing. The pre-summing step introduces a sinc^2 variation in echo power with increasing frequency, which we correct in the subsequent mapping.

III. Focused Mapping

Each observation tracks a particular target location on the Moon, the target point, specified by a latitude, θ_t, and longitude λ_t. As described in Section II, the time-varying range and range-rate for this point are corrected for in the transmitted signal, so that the echo from the target position arrives at the GBT at a fixed delay relative to the PRP and without a Doppler offset. For all other points on the Moon, however, the range and range-rate are changing with respect to the target point, with the rate of change increasing with distance from (θ_t, λ_t). A simple unfocused mapping of the radar echoes from the delay-Doppler coordinate system to a selenographic coordinate system will therefore lead to increasing smearing in resolution with distance from the target point. We employ a "patch focusing" algorithm to achieve the best possible spatial resolution across the region of the Moon illuminated by the 430-MHz Arecibo beam.

For almost all planetary radar observations, the beamwidths of the transmitting and receiving antennas (normally the same) are larger than the angular size of the solar system body being studied. This results in the so called north-south ambiguity; every location in one hemisphere of a rotating spherical body has a symmetric location in the other hemisphere which has the same distance and velocity relative to the radar [18]. For a single observation, the echo powers from each pair of locations cannot be separated. For our lunar observations the 9 arc min beamwidth of the Arecibo antenna at 430 MHz is smaller than the ~28 arc min angular diameter of the Moon, allowing the ambiguity problem to be largely avoided by limiting the illuminated area to one hemisphere of the Moon.

The relative motion of an observer on the Earth and a point on the Moon has components due to the intrinsic rotations of the two bodies, the librations of the Moon, and the geometry of the observer-target line with respect to these components (Figure 2). The sub-radar point (SRP), denoted by coordinates (θ_{srp}, λ_{srp}), lies at the intersection of the lunar surface with a line between the observer and the Moon's center of mass (COM). The SRP moves on the surface of the Moon throughout an observation period, and a plane containing two successive SRP vectors and the COM defines the instantaneous "Doppler equator". The vector perpendicular to this plane at the COM represents the apparent instantaneous rotation axis or "Doppler axis" of the Moon.

Contours of equal radar time delay form concentric circles about the SRP, which are also contours of equal incidence angle for a spherical reference surface. The Doppler shifts across the surface are well modeled by a spherical solid-body rotation, for which the apparent rate and axial tilt vary with time. We may therefore express the Doppler shift for any given lunar surface point as a function of the instantaneous SRP, apparent plane-of-sky rotation angle for the Doppler axis, γ, and the apparent maximum Doppler shift at the limbs (Hz), w.

We can compute detailed range and frequency (phase) histories for any individual surface location relative to the target point, but carrying this out for thousands of surface locations to achieve focused mapping would be computationally intensive. One solution is to acquire range and range-rate information, as a function of time, for several locations on the Moon. From these values, we determine a best-fit set of "spin" parameters at 1-minute intervals (θ_{srp}, λ_{srp}, w, γ), and fit a second-order polynomial to their variation with time. The errors between the actual frequency properties of the reference points and those

obtained by use of best-fit spin parameters are well below the values needed to create a one-pixel offset in the final selenographic maps.

The raw radar echoes are time-series samples of complex voltages denoted by $V(m, n)$, where m is the range bin and n denotes the particular pulse record. The target point echo occurs at a fixed range bin, m_t, in all records, and has zero frequency (or whatever arbitrary small offset value we introduce). To produce a focused delay-Doppler image about this point, we simply take the Fourier transform of the data along the columns (n) and resample to selenographic coordinates using the spin parameters (Section IV). No range compression is needed due to the use of a quasi-monochromatic signal. As the distance from the target location increases the range migration and Doppler offset over the 983 s coherence interval will also increase. The distance over which this offset becomes equal to the range and/or frequency resolution defines a "patch size" [7].

We build up the output map of a particular illuminated region by carrying out the frequency-transform operation and selenographic resampling for constituent patches, after applying a time-varying correction to the raw data array for delay and frequency variations between the original target point (θ_t, λ_t) and the center of the patch (a method suggested in [7]). The focusing operation is applied in four steps. (1) An interpolation of each range record (along the m samples) is used to correct the time-varying delay offset. These delay errors vary slowly with time, so we can apply a single correction to each pulse record. (2) The cumulative phase difference between the pointing target and patch center, the primary source of image smearing, is compensated at each pulse record of the complex voltage array, based on the spin state of the Moon at the start of the pulse. (3) The array is Fourier-transformed along the frequency lines to yield a delay-Doppler

array. (4) The relative backscatter intensity is mapped to selenographic coordinates across the patch, as detailed in the next section.

IV. Relationship of delay-Doppler and Selenographic Coordinates

The mapping between delay-Doppler and selenographic coordinates requires a transform between the Cartesian (*x, y, z*) location of a point on the lunar reference grid with latitude θ and longitude λ:

$$\begin{bmatrix} x \\ y \\ z \end{bmatrix} = r_{moon} \begin{bmatrix} \cos\theta\cos\lambda \\ \cos\theta\sin\lambda \\ \sin\theta \end{bmatrix} \quad (1)$$

and the (*x'', y'', z''*) coordinates along the axes that define the apparent (plane of sky) orientation and spin state of the Moon (Figure 2). The radius of the Moon at this location is given by r_{moon}. For most mapping, we assume a single mean radius for the Moon, but more detailed topography (if available) could be used to orthorectify the final image. The transformation is represented by:

$$[D][S]\begin{bmatrix} x \\ y \\ z \end{bmatrix} = \begin{bmatrix} x'' \\ y'' \\ z'' \end{bmatrix} \quad (2)$$

where [S] rotates the coordinate system to place the sub-radar point along the *x''* axis:

$$[S] = \begin{bmatrix} \cos\lambda_{srp}\cos\theta_{srp} & \sin\lambda_{srp}\cos\theta_{srp} & \sin\theta_{srp} \\ -\sin\lambda_{srp} & \cos\lambda_{srp} & 0 \\ -\cos\lambda_{srp}\sin\theta_{srp} & -\sin\lambda_{srp}\sin\theta_{srp} & \cos\theta_{srp} \end{bmatrix} \quad (3)$$

The [D] matrix rotates the coordinates about the *x''* axis by the Doppler angle (defined as positive clockwise), γ:

$$[D]=\begin{bmatrix}1 & 0 & 0\\ 0 & \cos\gamma & -\sin\gamma\\ 0 & \sin\gamma & \cos\gamma\end{bmatrix} \quad (4)$$

Delay variations arise due to differences in the range of a surface point at (*x''*, *y''*, *z''*), R_T, with respect to the SRP range, R_{srp}. This difference in range is given by:

$$\Delta r = R_T - R_{srp} = \left[R_{srp}^2 + 2r_{moon}^2 + 2R_{srp}r_{moon} - 2x''(R_{srp} + r_{moon})\right]^{1/2} - R_{srp} \quad (5)$$

and the appropriate delay bin is:

$$n\_delay = m_o - \frac{2\Delta r}{\Delta tc} \quad (6)$$

where c is the speed of light and Δt is the delay resolution. The value of *x''* must be >0 in order for the desired point to be on the radar-visible hemisphere of the Moon. The radar incidence angle, ϕ, is:

$$\phi = \cos^{-1}\left(x''/r_{moon}\right) \quad (7)$$

The frequency bin, in the transformed data array, for a surface point at (*x''*, *y''*, *z''*) is:

$$n\_freq = T_{coh}\left(f_o + y'' * w/r_{moon}\right)\frac{(R_{srp} + r_{moon})}{R_T} \quad (8).$$

We re-project the radar data by solving for the appropriate delay and frequency bin in the Fourier-transformed array for each (latitude, longitude) cell in the output map. These output values may be complex-valued, if we wish to later form a Stokes vector representation of the echo, or converted to relative power by taking the squared magnitude of the complex values.

The surface horizontal resolution along the range axis is a function of the incidence angle:

$$\Delta s_{range} = \Delta r / \sin\phi = \frac{c\Delta t}{2\sqrt{1-\left(\frac{x''}{r_{moon}}\right)^2}} \quad (9)$$

and for our 3-μs observations varies from 450 m at the limbs to 900 m at 30° incidence. The horizontal resolution along the axis perpendicular to the range direction ("azimuth"), $\Delta s_{\text{azimuth}}$, is best when the image area is close to the Doppler axis (y"=0):

$$s_{azimuth} = \frac{r_{moon}}{wT_{coh}\sqrt{1-\left(\frac{y''}{r_{moon}}\right)^2}} \quad (10)$$

The surface area, A, contributing to the echo in a given delay-Doppler cell is thus:

$$A = \frac{r_{moon}c\Delta t}{2wT_{coh}\sqrt{1-\left(\frac{x''}{r_{moon}}\right)^2}\sqrt{1-\left(\frac{y''}{r_{moon}}\right)^2}} \quad (11)$$

For the 983-second looks, the finest azimuth horizontal resolution is ~320 m. Farther from the axis, the azimuth resolution cells increase in size, and at the Doppler equator (where the azimuth and range axes are parallel) there is no useful frequency mapping capability. The final maps are produced at 400 m resolution to limit under-sampling of the frequency-resolved cells.

V. Calibration and Multi-Look Averaging

One advantage of our 70-cm radar mapping, relative to shorter-wavelength observations using the same antennas, is the large illuminated region on the Moon. This permits acquisition of full nearside coverage, with 3 or more looks, in only ~20 "runs" (one 2-2.5 hour passage of the Moon above Arecibo) with different target locations. There is, however, a variation in effective gain across the illuminated region (Figure 1),

which must be removed to mosaic data for adjacent target areas. The true beam pattern varies with time during a run, because the Arecibo 430-MHz line feed illuminates a toroidal region of the dish, and progressively spills off the edge of the fixed reflector as the elevation angle decreases. The GBT antenna has a fixed sensitivity pattern, as it tracks the target point. The net round-trip power beam pattern, $P(\kappa)$, for a summed set of looks can be represented by a Bessel function with an "effective width" parameter, W:

$$P(\kappa) = \left[J_1(2W\pi\sin\kappa)/(W\pi\sin\kappa)\right]^4 \tag{12}$$

where κ is the angle between the pointing target and a chosen surface point [20]. In the case of a fully illuminated aperture at Arecibo (i.e. when pointing at the zenith), the net beam pattern is well represented by W=170. Lower values correspond to wider beams as the illuminated area decreases with decreasing elevation angle. The beam angle may be defined from the plane-of-sky offsets in the rotated coordinate system, and the observer-target distance, R_T:

$$\kappa = \tan^{-1}\left(\frac{\sqrt{\left(y'' - y''_{target}\right)^2 + \left(z'' - z''_{target}\right)^2}}{R_T}\right) \tag{13}$$

The average beam pattern for the Arecibo-GBT 70-cm data is given by W=155, based on analysis of overlap regions between images collected for different pointing centers. The resulting correction factor is used to normalize the σ^o values for their distance from the beam center.

Each radar look includes time samples that contain no reflections from the Moon. In this region, the measured power equals the product of the net system gain in each channel, G_1 and G_2, and the net thermal noise from the receiver system and the Moon plus background sky noise since the degree to which the Moon fills the GBT beam varies

with the target location. The lunar and sky emissions are assumed to be the same in the two circular polarizations. Where lunar echoes are present, the measured power contains both the noise and the lunar echo power. The dimensionless backscatter coefficient, σ^o, may be expressed in terms of the average transmitted power, P_T, the thermal noise power, P_N, the scattering area, A, the gain of the transmitting and receiving antennas, G_{AO} and G_{GBT}, the range between the target and the observer, R_T, and the ratio of the observed echo power (i.e. after the off-Moon noise power has been subtracted) at some location in the radar image, S_{image}, to that in the off-Moon region, $S_{off\text{-}Moon}$:

$$\sigma^o = \frac{S_{image}}{S_{off-Moon}} \left(\frac{P_N}{P_T} \right) \left(\frac{1}{A} \right) \left[\frac{64\pi^3 R_T^4}{\lambda^2 G_{AO} G_{GBT}} \right] \quad (14)$$

The noise power is given by kT_BB_N, where k is Boltzmann's constant, T_B is the system temperature of the GBT at 430 MHz, and B_N is the noise bandwidth.

The system temperature varies with the degree to which the Moon fills the GBT beam, so we measured this parameter as a function of incidence angle for the center of the pointing region (i.e., from the center of the Moon to the limbs). We also observed a sky source of known flux at 430 MHz to determine the absolute brightness temperature. As expected, the brightness temperatures were very similar between the left- and right-circular polarization receivers, and the average value is 166 K for pointing locations with $\phi < 25^o$. At higher angles, the beam is partially off the Moon, and a good approximation to the GBT system temperature is:

$$T_{system}^{GBT} = 415\phi^{-0.289} \text{ (for } \phi > 25^0) \quad (15)$$

Targets very close to the limb thus have a 430-MHz noise temperature of ~113 K (Figure 3).

The noise bandwidth is very close to the frequency resolution, 1 mHz. The gain of the GBT at 430 MHz is a fixed value, 51.5 dB, but the dependence of the illuminated area on the Arecibo primary reflector on zenith angle leads to a reduction in gain with zenith angle, α in degrees [P. Perillat, pers. comm.]:

$$G_{AO} = \left(\frac{11044\,\pi}{\lambda^2}\right)\left[18.67 - 0.5414\,\alpha\right] \tag{16}$$

Using these corrections, derived σ^o values in spatially overlapping regions of observations with different target locations ("runs") differ by ±3 dB. Our greatest uncertainty in calibrating the backscatter coefficient is the transmitted power, which is not well measured at Arecibo. These differences between different observing runs can be compensated to produce mosaics of large areas (Figure 4), but the absolute backscatter coefficient remains uncertain by about 50%. The relative cross sections between the two circular polarizations are known with much higher accuracy. We normalize the PDS "Level 2" data products to the measured 68-cm scattering functions in [21] to reduce the strong dependence of echo brightness on incidence angle (Table 1).

In order to decrease speckle in the final radar maps, we collect three or more independent looks at each target area. Each look is mapped using the patch-focusing method above. The standard deviation of the relative power values due to speckle is reduced by incoherent summation as $1/\sqrt{N}$, where N is the number of averaged looks. While 3-8 summed looks yield a geologically useful radar map, we typically require a higher degree of local averaging (~100 looks) in order to reduce the uncertainties in the circular polarization ratio (SC/OC power).

Slight image distortions between looks are corrected by selecting a single look as a "reference" image, and choosing widely spaced tie-points within this image. For each

succeeding look, we determine through cross-correlation a best offset (Δx, Δy) for each tiepoint, apply a rubbersheet transformation, and sum the data. Data being archived with the NASA Planetary Data System (PDS) at "Level 2" have also been geometrically corrected to match the Clementine 750-nm optical image base (Table 1).

VI. Relationship of Radar Echoes to Mare Basalt Age and Ilmenite Content

Basins on the lunar near side, formed by giant impacts more than 2.8 b.y. ago, are largely filled by basaltic lava flows called maria. These flow complexes formed as low relief plains, and have been subsequently covered by an impact-produced mixture of rocky debris and dust called the regolith. Considerable work has been done to understand mare composition and age, since these reveal the thermal and chemical history of the magma reservoirs that supplied the eruptions. There are two principal sources of remote sensing information on mare flow composition: near-infrared multi-spectral properties and orbital gamma-ray/neutron spectroscopy. Relative dating is accomplished by studying the abundance and degradation state of impact craters, with absolute dating by reference to "standard" population curves for areas surrounding samples of known age. A recent study [22] applied these techniques to spectroscopically-defined units across virtually all nearside maria.

Long-wavelength radar data can play a complementary role in these investigations. Schaber et al. [10] noted that 70-cm radar echoes for lava flows in Mare Imbrium were typically lower for flows that are "blue", or higher in their abundance of the mineral ilmenite ($FeTiO_3$). This mineral has a higher microwave loss tangent than other species in mare basalts, and much higher loss than the generally feldspar-rich rocks that form the

lunar highlands; work on returned lunar samples confirmed that the loss properties of basalts are correlated with the total iron and titanium content [23]. Since much of the 70-cm radar return comes from scattering within the regolith, an increased loss tangent leads to lower echoes by attenuating the incident signal [24].

Comparison of 4-8 km resolution 70-cm radar images with FeO and TiO_2 abundance estimated from multispectral data showed that the TiO_2 (i.e., ilmenite) content appears to be the principal driver of basalt loss tangents, with other iron-bearing minerals playing a much less significant role [11]. This same study identified differences in overall radar brightness between the maria in major basins for any given TiO_2 abundance, and suggested that such variations might be linked to relative age. In this model, supported by measurements of the thermal properties of the maria during eclipse, younger mare units have a thin (2-3 meters) regolith cover, which permits relatively small impacts to excavate fresh blocky debris from the underlying bedrock. With greater age, the regolith thickens to 5-8 m, and small impacts simply break down the existing suspended boulders. As a result, a younger mare unit will have higher radar brightness (more surface and suspended rocks to permit volume scattering) than an older unit of the same TiO_2 content (Figure 5). Our new 70-cm radar maps permit a more detailed comparison between echo properties, inferred composition, and crater-statistic age estimates.

We selected Mare Serenitatis (Figure 6a) for a preliminary study, as the entire basin is contained within a single beam pattern of the 70-cm system (Figure 6b). This avoids any issues of relative calibration between images collected with different target centers. Serenitatis basalts were mapped based on differences in infrared reflectance by Pieters [25], and in an early form by Thompson et al. [26]. We mapped the FeO (Figure 6c) and

TiO_2 (Figure 6d) abundance using Clementine data and the techniques of Lucey et al. [27] and Gillis et al. [28].

Mare Serenitatis is characterized by an inner area of lower titanium and iron basalts, surrounded by a concentric ring of moderate to high-titanium flows. Many of the abrupt changes in TiO_2 between flow complexes are accompanied by changes in the same-sense radar echoes, consistent with our expectation that ilmenite modulates the regolith loss tangent. A comparison of the radar image and TiO_2 map, however, also shows some dramatic differences. Most striking is a "finger" of radar-bright material extending northward from the area of Bessel crater. This higher radar return is not accompanied by a change in the iron or titanium maps. In the area northwest of Posidonius crater, a relatively homogenous area of moderate-TiO_2 flows comprises distinct areas of moderate and very low radar return. Across the entire Serenitatis basin, the radar echoes appear to trace "unit" boundaries that are often somewhat different from those that are readily noted in the TiO_2 map or in earlier multi-spectral characterizations [25].

To quantify these differences, we compared the average same-sense radar brightness to the average TiO_2 abundance for 21 sample areas with relatively uniform properties (Figure 7). Excluding the very radar-dark area north of Posidonius crater, the results cluster about a trend line with an approximate slope of -0.3 dB per 1% increase in TiO_2 abundance. This is consistent with about one-half of the scattered 70-cm signal arising from subsurface reflections, per the model of [14]. There are discrepancies from this simple relationship, particularly for the area north of Posidonius and a number of moderate-TiO_2 (6-9%) basalt units with anomalously high radar echoes.

The new 70-cm data support previous work suggesting a strong anti-correlation between mare basalt ilmenite content, inferred from multi-spectral data, and same-sense radar echo strength [10, 11]. In greater detail, however, the radar echoes also offer complementary information to the optical and near-infrared observations. The discrepancies in radar return from a simple trend with TiO_2 may arise from: (1) variations in relative age among units of relatively similar composition, where the radar echo discriminates age differences due to regolith depth and rock abundance (Figure 5); (2) variations in mineralogy among the basalt flows that affects the microwave loss tangent without a discernable change in the FeO or TiO_2 abundance. We have, at present, no evidence for such a mineralogical mechanism based on lab studies of lunar samples [24], so relative age differences appear to be the most plausible explanation.

The age of major mare deposits in Serenitatis have been estimated [23] based on impact crater statistics. As a general rule, such ages are most robust where large regions are studied, and have greater possible errors for smaller areas. The radar data may provide a means for refining these age estimates for relatively small deposits. Our best example of a unit potentially older than expected is the feature north of Posidonius, within the unit termed S8 by Heisinger et al. [22] and dated to 3.63 b.y. (Figure 8). The radar echo is 6 dB below that expected from the σ^o-TiO_2 trend, suggesting that this deposit may be closer to the high end of Serenitatis basalt ages. A possible unit with younger age than expected is the southeastern part of unit S15, estimated at 3.44 b.y. [22] (labeled in Figure 6a). In the southeast portion, the radar echo is 5 dB higher than predicted from the TiO_2 content, suggesting that the age of the materials near the basin

rim is considerably younger than that of the more interior deposits of similar spectral properties.

It appears that the 70-cm radar data can play a significant role in refining the mapping of mare unit boundaries and their relative age. Further work is needed to examine crater counts in relatively large areas of uniform TiO_2 content, and to then compare these ages against the average radar echo behavior to define a relationship between σ^o, TiO_2, and age. If this technique proves valid, then the radar data and inferred composition could be used to define relative ages for mare outcrops too small for robust crater statistics.

Conclusions

The new 70-cm wavelength radar maps have application to a wide variety of problems including lunar geologic history and the resource potential of mare basalts, explosive pyroclastic deposits, and polar cold traps [29]. These data are being archived with the NASA Planetary Data System to make them available to the lunar science community.

Acknowledgment

This work was supported in part by a grant from NASA's Planetary Astronomy Program. The authors thank the staff at Arecibo Observatory and the Greenbank Telescope for invaluable assistance in collecting the lunar radar data. In particular, we thank F. Ghigo at Green Bank and A. Hine of the Arecibo Observatory. The Arecibo Observatory is part of the National Astronomy and Ionosphere Center, which is operated by Cornell University under a cooperative agreement with the National Science Foundation (NSF). The Green Bank Telescope is part of the National Radio Astronomy

Observatory, a facility of the NSF operated under cooperative agreement by Associated Universities, Inc.

References

[1] Zisk, S.H., Pettengill, G.H. and Catuna, G.W. 1974. High-resolution radar maps of the lunar surface at 3.8-cm wavelength. The Moon, 10, 17-50.

[2] Thompson, T.W. 1987. High resolution lunar radar map at 70-cm wavelength. Earth Moon Planets, 37, 59-70.

[3] Thompson, T.W. 1978. High resolution lunar radar map at 7.5 m wavelength. Icarus, 36, 174-188.

[4] Zisk, S.H., Campbell, B.A., Pettengill, G.H. and Brockelman, R. 1991. Alphonsus crater: Floor fracture and dark-mantle deposit distribution from new 3.0-cm radar images. Geophys. Res. Letters, 18, 2137-2140.

[5] Margot, J.L., Campbell, D.B., Jurgens, R.F. and Slade, M.A. 1999. Topography of the lunar poles from radar interferometry: A survey of cold trap locations. Science, 284, 1658-1660.

[6] Margot, J.L., Campbell, D.B., Jurgens, R.A., and Sade, M.A. 2000. Digital elevation models of the Moon from Earth-based radar interferometry. IEEE Trans. Geosci. Rem. Sensing, 38, 1122-1133.

[7] Stacy, N.J.S. 1993. High-resolution synthetic aperture radar observations of the Moon. Ph.D. Thesis, Ithaca, NY: Cornell University.

[8] Stacy, N.J.S., Campbell, D.B. and Ford, P.G. 1997. Radar mapping of the lunar poles: A search for ice deposits. Science, 276, 1527.

[9] Campbell, D.B., B.A. Campbell, L.M. Carter, J.L. Margot, and N.J.S. Stacy, Lunar polar ice: No evidence for thick deposits at the south pole, Nature, *in press*, 2006.

[10] Schaber, G.G., Thompson, T.W. and Zisk, S.H. 1975. Lava flows in Mare Imbrium: An evaluation of anomalously low Earth-based radar reflectivity. The Moon, 13, 395-423.

[11] Campbell, B.A., Hawke, B.R. and Thompson, T.W. 1997. Long-wavelength radar studies of the lunar maria. J. Geophys. Res., 102, 19,307-19,320.

[12] Thompson, T.W., Roberts, W.J., Hartmann, W.K., Shorthill, R.W. and Zisk, S.H. 1979. Blocky craters: Implications about the lunar megaregolith. Moon and Planets, 21, 319-342.

[13] Ghent, R.R., D.W. Leverington, B.A. Campbell, B.R. Hawke, and D.B. Campbell, Earth-based observations of radar-dark crater haloes on the Moon: Implications for

regolith properties, *J. Geophys. Res*., Vol. 110, No. E2, E02005, DOI10.1029/2004JE002366, 2005.

[14] Campbell, B.A., and B.R. Hawke, Radar mapping of lunar cryptomaria east of Orientale basin, *J. Geophys. Res*., doi:10.1029/2005JE002425, 2005.

[15] Zisk, S.H. et al. 1977. The Aristarchus-Harbinger region of the Moon: Surface geology and history from recent remote sensing observations. The Moon, 17, 59-99.

[16] Gaddis, L.R., Pieters, C.M. and Hawke, B.R. 1985. Remote sensing of lunar pyroclastic mantling deposits. Icarus, 61, 461-489.

[17] Campbell, B.A., Stacy, N.J., Campbell, D.B., Zisk, S.H. and Thompson, T.W. 1992. Estimating lunar pyroclastic deposit depths from imaging radar data: Applications to lunar resource assessment, Workshop on New Technologies for Lunar Resource Assessment, LPI Tech Report 92-06, 16-17.

[18] Pettengill, G.H., Zisk, S.H. and Thompson, T.W. 1974. The mapping of lunar radar scattering characteristics. The Moon, 10, 3-16.

[19] Margot, J.L. 2002. A portable fast sampling system for astronomical applications. Proc. URSI Gen. Assembly, Maastricht.

[20] Skolnik, M.L. 1980. Introduction to Radar Systems. New York: McGraw-Hill.

[21] Hagfors, T. 1970. Remote probing of the Moon by infrared and microwave emissions and radar. Radio Science, 5, 189-227.

[22] Heisinger, H., R. Jaumann, G. Neukum, and J.W. Head 2000. Ages of mare basalts on the lunar nearside, J. Geophys. Res., 105, 29,329-29,275.

[23] Carrier, W.D., Olhoeft, G.R. and Mendell, W., 1991. Physical properties of the lunar surface. In: Lunar Sourcebook. Cambridge Univ. Press, New York.

[24] Thompson, T.W., Pollack, J.B., Campbell, M.J. and O'Leary, B.T. 1970. Radar maps of the Moon at 70-cm wavelength and their interpretation. Radio Science, 5, 253-262.

[25] Pieters, C.M., 1978. Mare basalt types on the front side of the Moon. Proc. Lunar Plan. Sci. Conf. 9, 2825-2849.

[26] Thompson, T.W., R.W. Shorthill, E.A. Whitaker, and S.H. Zisk 1974, Mare Serenitatis: A preliminary definition of surface units by remote observations, The Moon, 9, 89-96.

[27] Lucey, P.G., D.T. Blewett, and B.D. Joliff, 2000, Lunar iron and titanium abundance algorithms based on final processing of Clementine UV-Visible images, J. Geophys. Res., 105, 20,297-20,306.

[28] Gillis, J.J., B.L. Joliff, and R.C. Elphic, A revised algorithm for calculating TiO_2 from Clementine UVVIS data: A synthesis of rock, soil, and remotely sensed TiO_2 concentrations, *J. Geophys. Res., 108*, doi:10.129/2001JE001515, 2003.

[29] Campbell, B.A., and D.B. Campbell 2006, Surface properties in the south polar region of the Moon from 70-cm radar polarimetry*, Icarus*, 180, 1-7.

Table 1. Description of NASA Planetary Data System Archive Products

PDS Level	Radiometric Corrections	Cartographic Corrections	Map Projections
1	Power in each pixel normalized to scattering area on the lunar surface and GBT thermal noise level.	Individual looks co-registered to correct minor offsets.	Sinusoidal equal-area and polar stereographic.
2	Power in each pixel normalized to backscatter coefficient using measured transmitter power, beam pattern, and Arecibo gain function. Values of backscatter coefficient further normalized by average angular scattering properties of lunar surface.	Images warped to match Clementine 750-nm basemap.	Sinusoidal equal-area and polar stereographic.

Figure Captions

Figure 1. An unfocused, 70-cm wavelength, delay-Doppler (range-rate) image of the Moon, showing the radar illumination pattern on the surface. Dark ellipse is the first null of the Arecibo antenna beam pattern. The radar beam was pointed at the center of Mare Orientale (the dark region in the center of the Orientale basin). Portions of the mountainous basin ring can be seen beyond the apparent limb of the Moon due to their higher elevation.

Figure 2. Schematic of apparent lunar range and range rate ("Doppler") coordinate system. Line from center of mass through sub-radar point defines the delay axis, x''. Plane of sky contains apparent spin axis, z''. Third Cartesian axis, y'', corresponds to changes in the apparent range rate or Doppler shift. Doppler "equator" lies in the $x'' - y''$ plane; there is an ambiguity between delay and Doppler coordinates of points north and south of this plane. Radar incidence angle, ϕ, is defined with respect to the x'' axis. Relationship between this apparent coordinate system and the lunar cartographic grid (latitude, longitude) is discussed in text.

Figure 3. Greenbank Telescope 430-MHz system temperature (K), which includes both the lunar surface emission and background sky contributions, versus incidence angle for targets on the Moon. System temperature about 166 K at center of Moon, and ~113 K when pointed at the limb. There is almost no dependence of lunar physical temperature

on lunation at this wavelength. Solid line shows best-fit power-law function of incidence angle, for angles >25^{o}.

Figure 4. 70-cm wavelength, same-sense polarization radar image mosaics of the nearside and limb regions of the Moon. Radar echoes are normalized to a cosine variation of power with incidence angle. Logarithmic scaling with black-white dynamic range of 45 dB. Horizontal spatial resolution averaged to about 1.2 km per pixel. Simple cylindrical projection used for equatorial regions. (a) 70 S – 0 latitude; 110 W - 0 W longitude; (b) 70 S – 0 N latitude, 0 E -110 E longitude; (c) 0 N – 70 N latitude, 0 E - 110 E longitude; (d) 0 N – 70 N latitude, 0 W -110 W longitude; (e) polar stereographic projection of north polar region (60-90^{o} N latitude). Zero longitude is toward bottom; (f) polar stereographic projection of south polar region (60-90^{o} S latitude). Zero longitude is toward top. Note that the Moon's libration during the period 2002-2006 predominantly favored viewing of the southern hemisphere from Arecibo. As a result, spatial coverage of the northern hemisphere is more limited in longitude.

Figure 5. Schematic of radar scattering in the mare regolith. Younger mare regolith is thinner (2-3 m), with larger population of suspended and surface decimeter-scale rocks. Older mare regolith is thicker (5-8 m), and has fewer rocks capable of supporting 70-cm radar scattering.

Figure 6. (a) Clementine 750-nm mosaic of Mare Serenitatis – grid lines 10^{o} (303 km) apart. Region covered is 12.8^{o}-39.8^{o} N, 3.1^{o}-35.3^{o} E; (b) 70-cm SC-polarized radar image

of Mare Serenitatis; (c) Map of TiO_2 content across Serenitatis using Clementine multi-spectral data and the technique of Gillis et al. [2003]; black-white stretch corresponds to values of 0-15%; (d) Map of FeO content across Serenitatis using Clementine multi-spectral data and the technique of Lucey et al. [2000]; black-white stretch corresponds to values of 0-25%.

Figure 7. Plot of radar backscatter versus TiO_2 content for basalts in Mare Serenitatis. Solid line shows best-fit trend for all areas except the radar-dark region north of Posidonius. Slope of trend line is about –0.3 dB per weight percent TiO_2.

Figure 8. Lunar Orbiter IV view of area north of Posidonius crater (95 km diameter), and (inset) 70-cm same-sense radar image of similar area, showing very low backscatter from an apparently older mare flow unit. White arrows show crater locations in both images for reference.

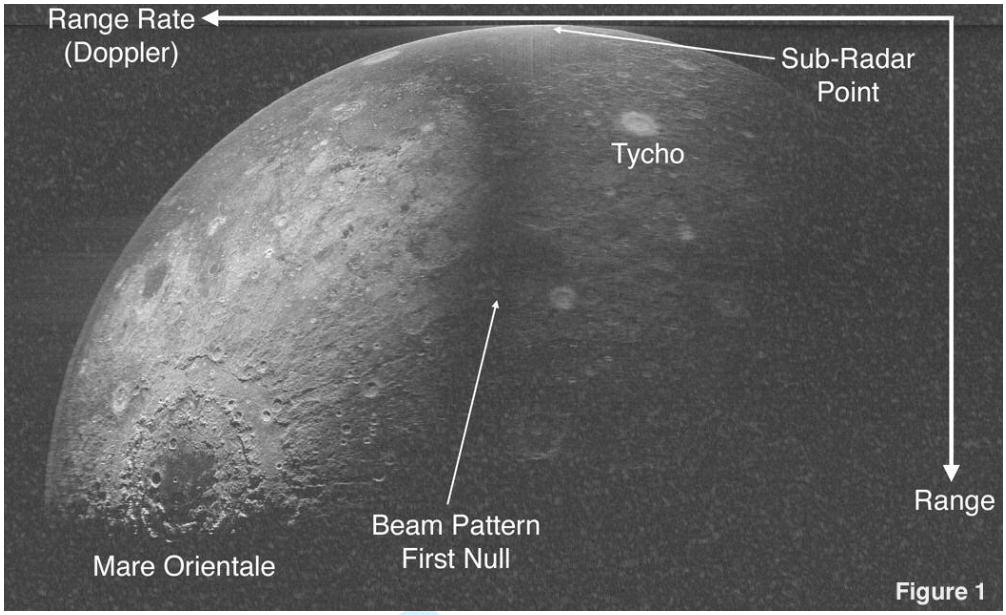

Figure 1

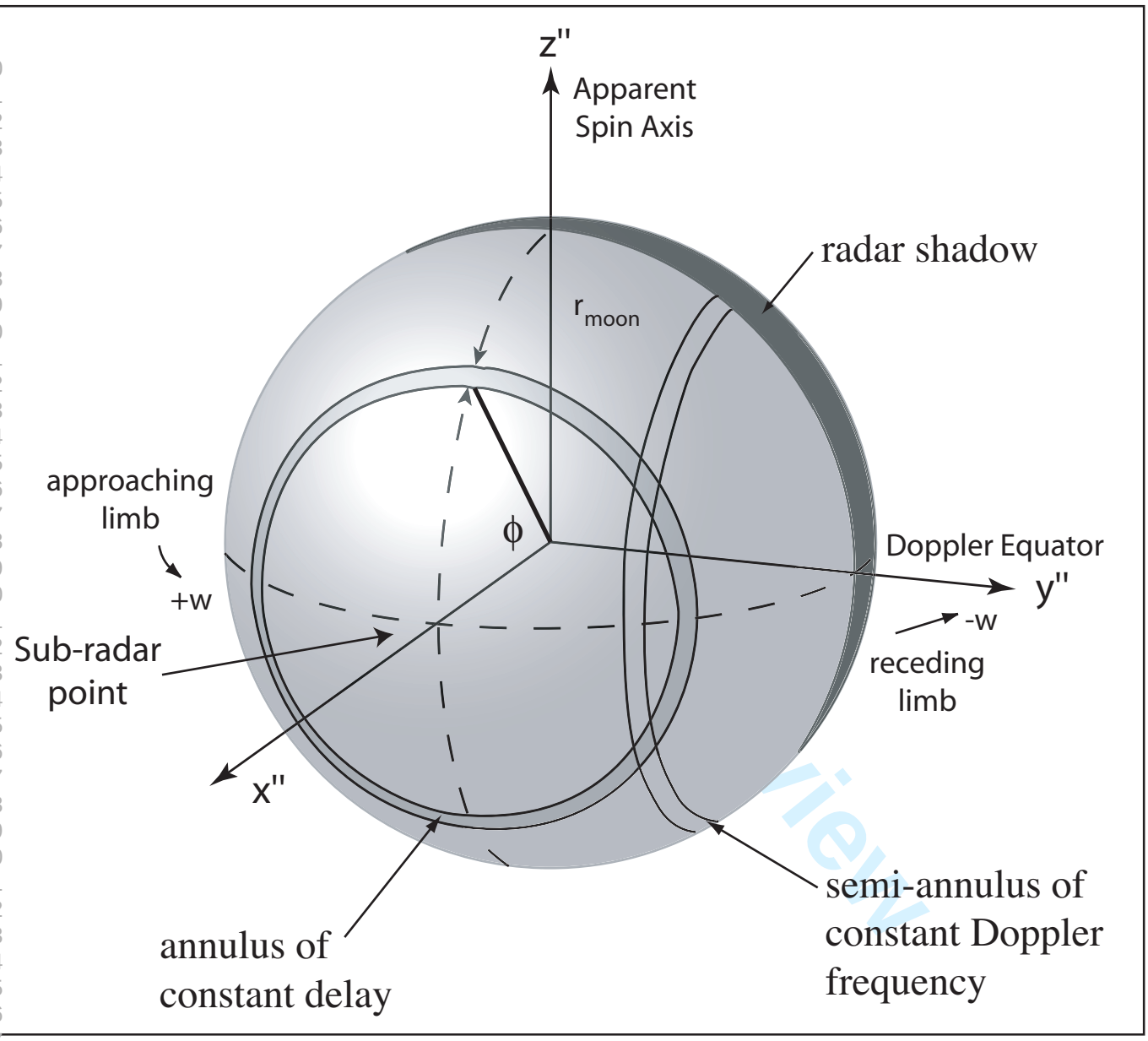

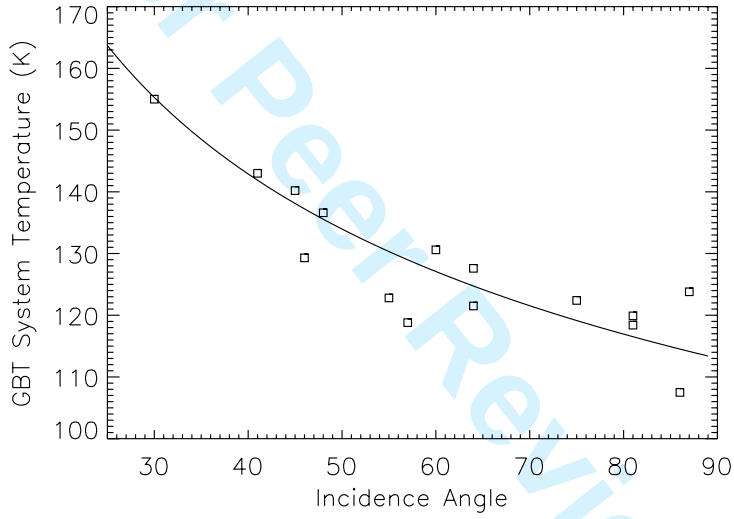

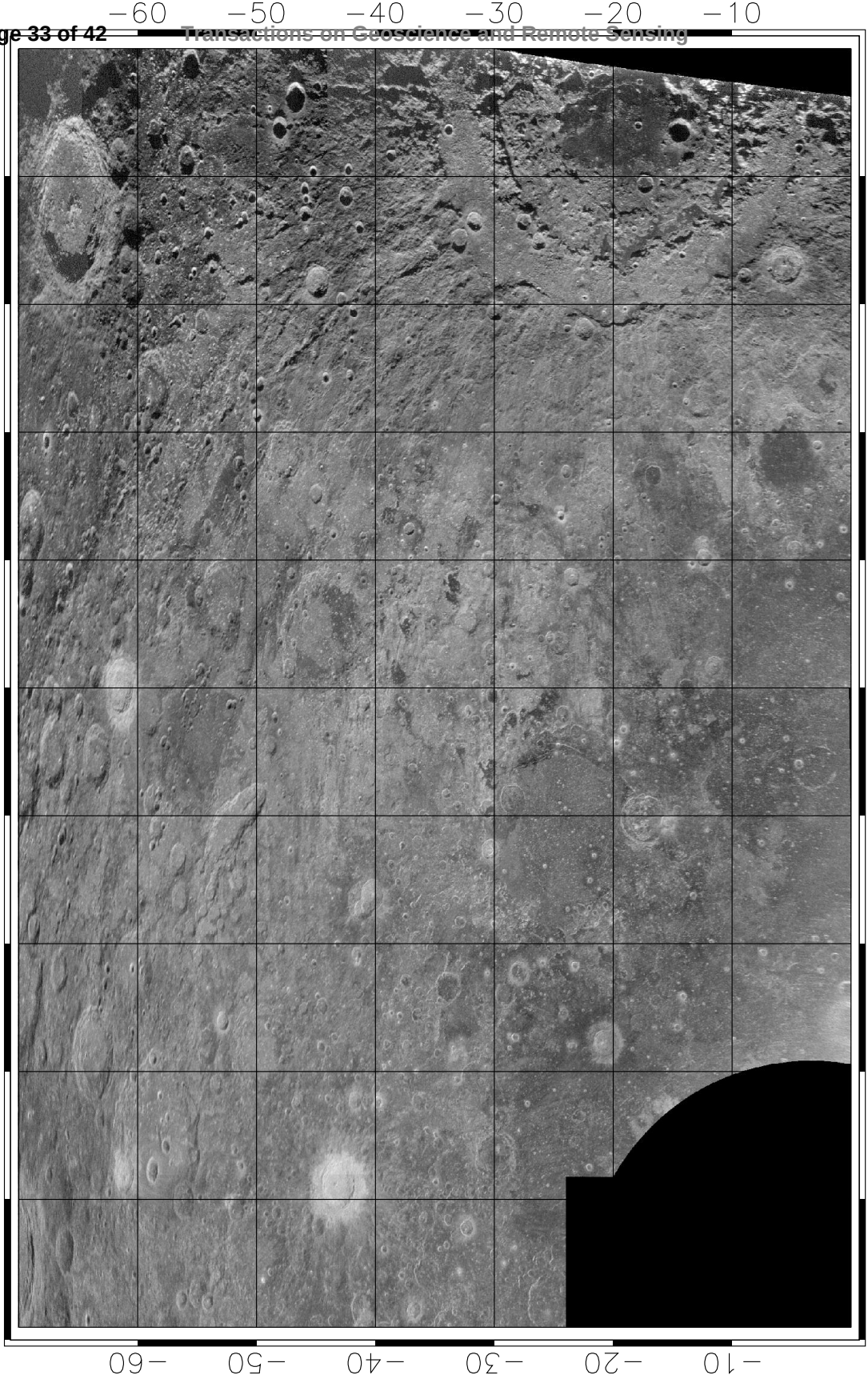
−60
−50
−40
−30
−20
−10
−90
−80
−70
−60
−50
−40
−30
−20
−10

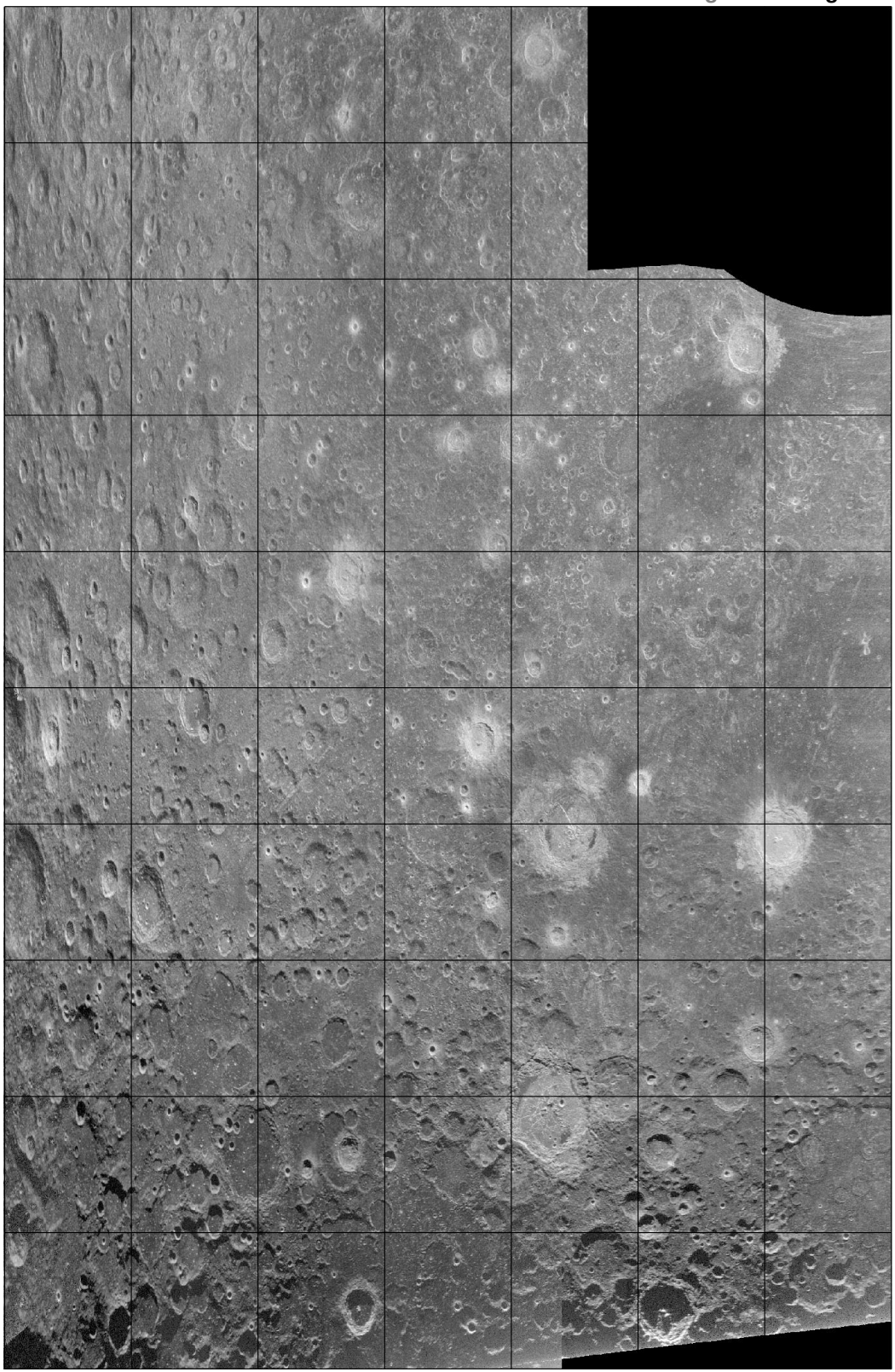
−60
−50
−40
−30
−20
−10
10
20
30
40
50
60
70
80
90

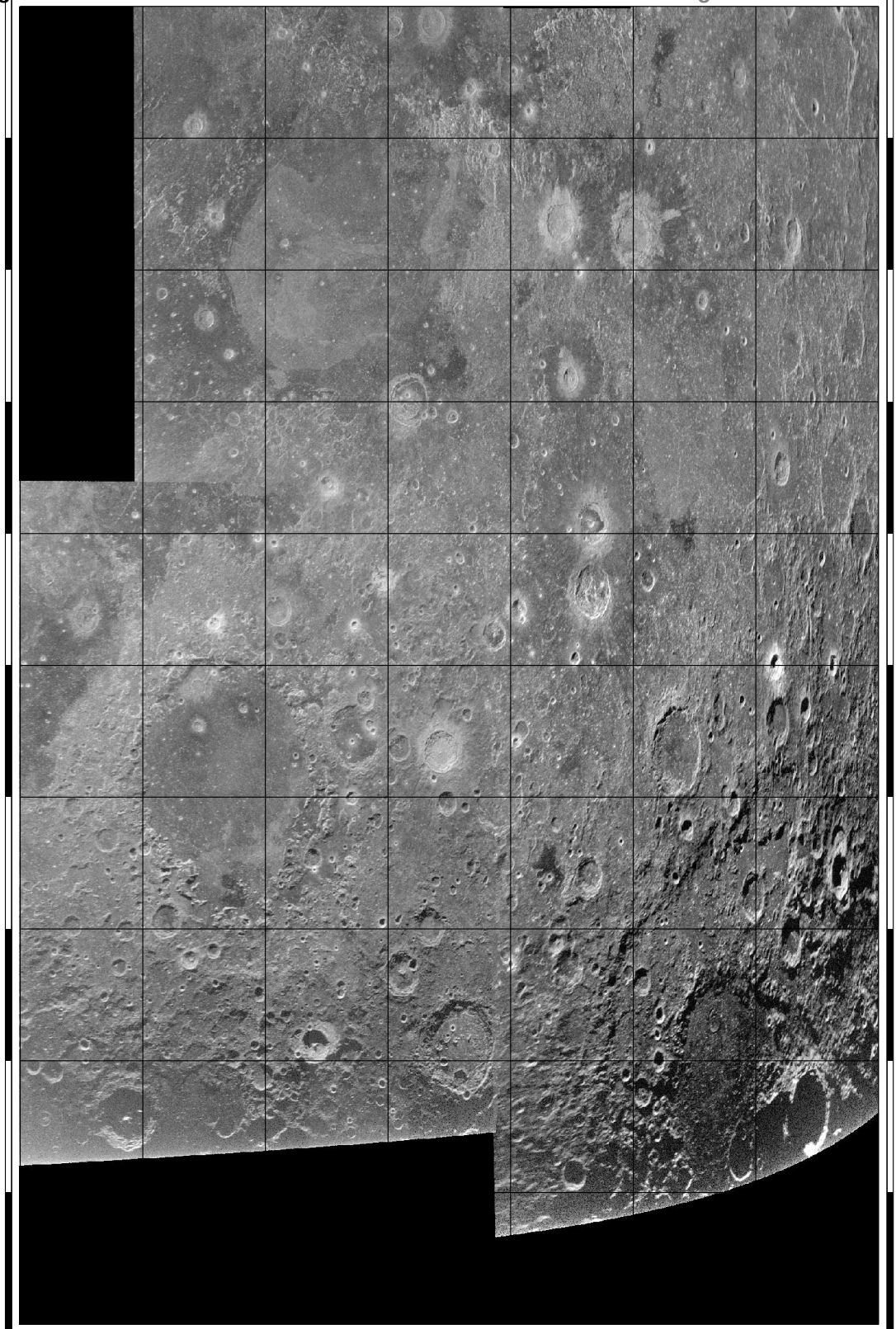

10
20
30
40
50
60
−90
−80
−70
−60
−50
−40
−30
−20
−10

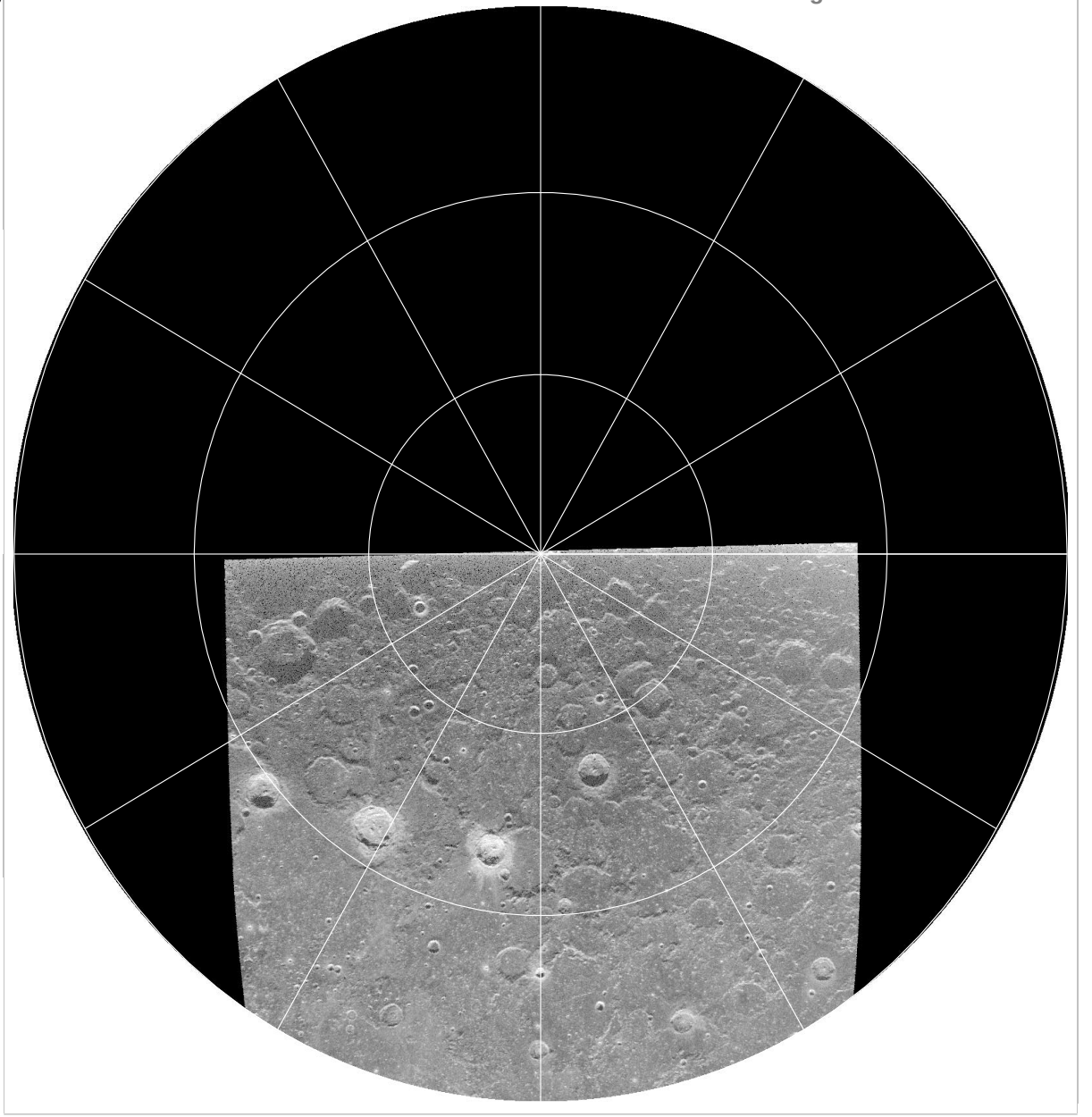

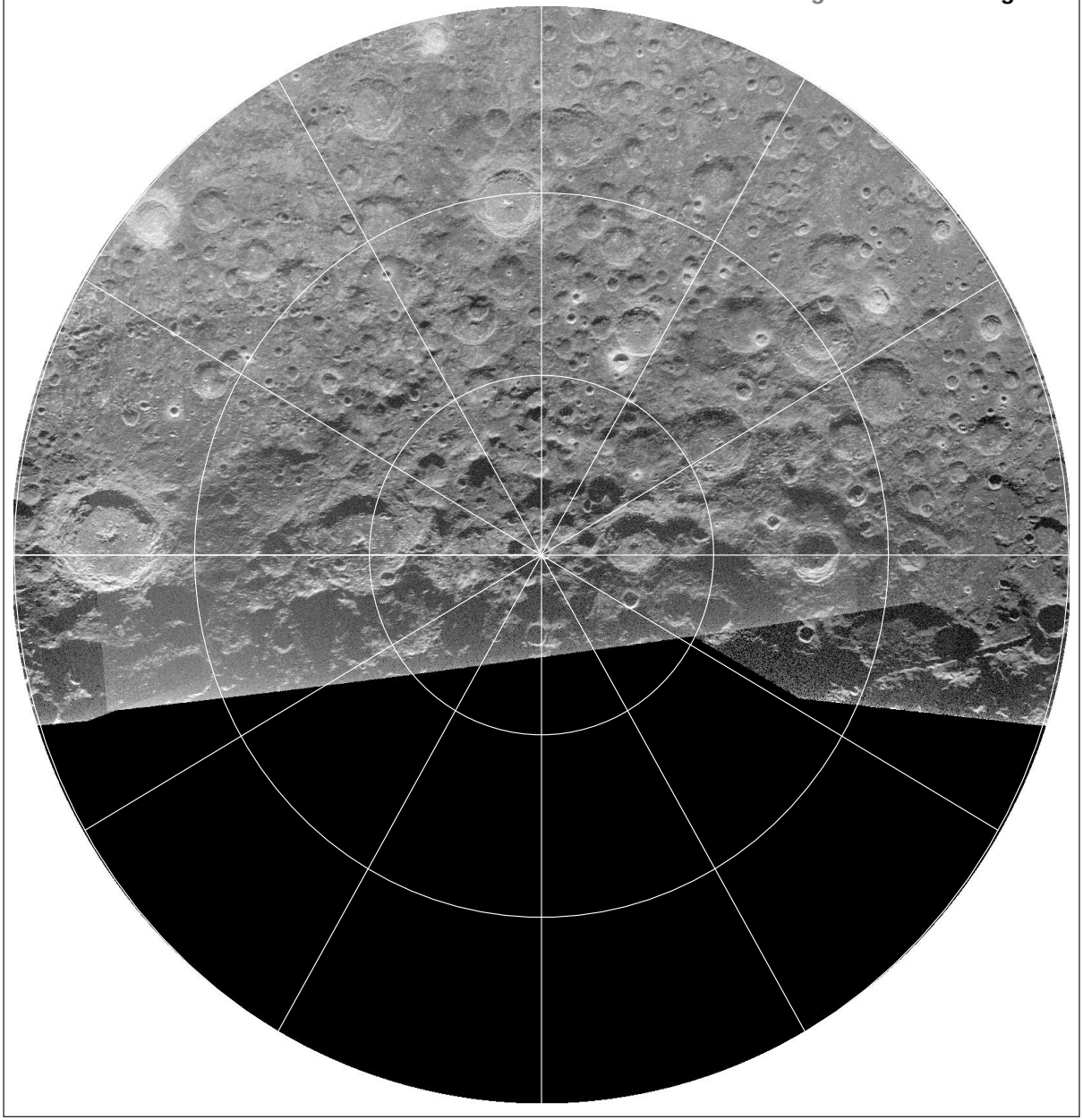

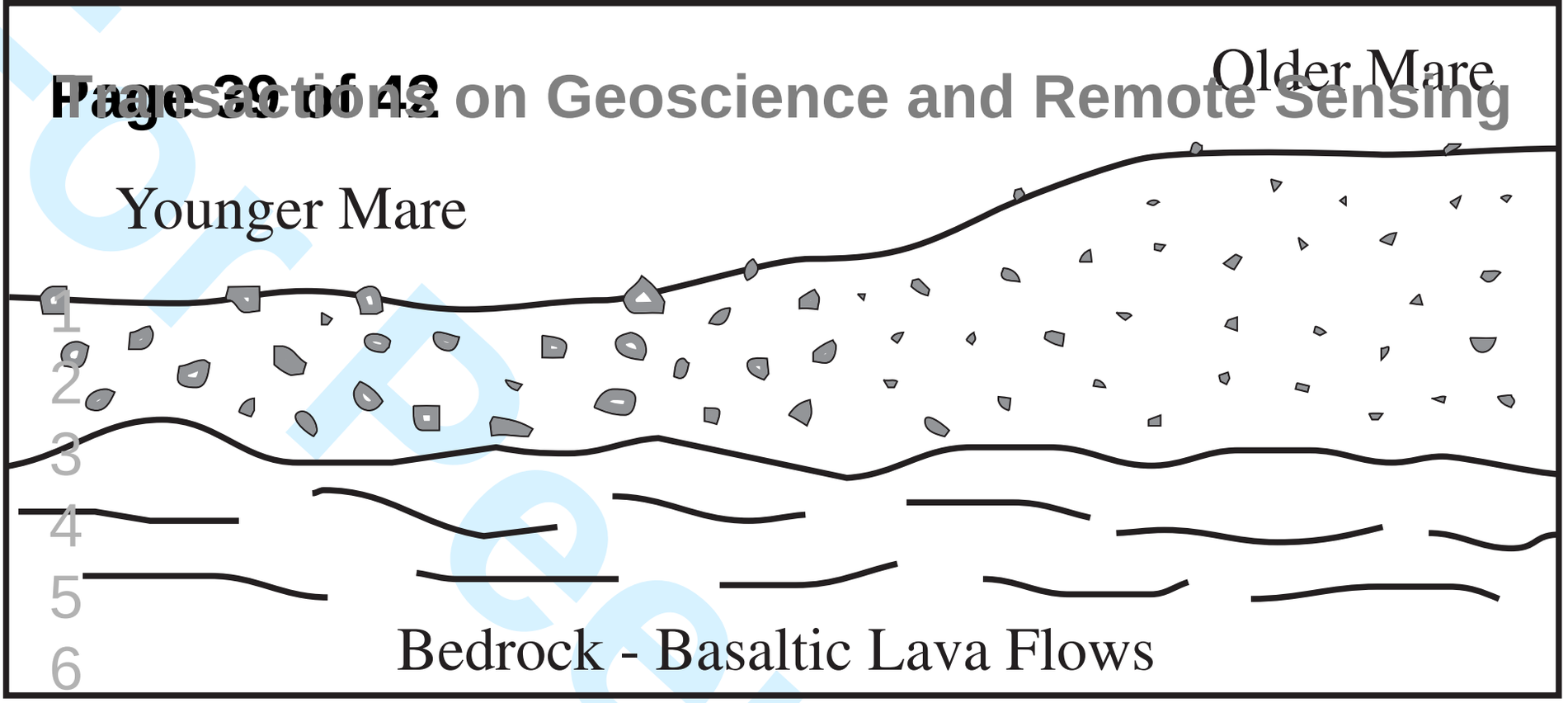

Figure 5

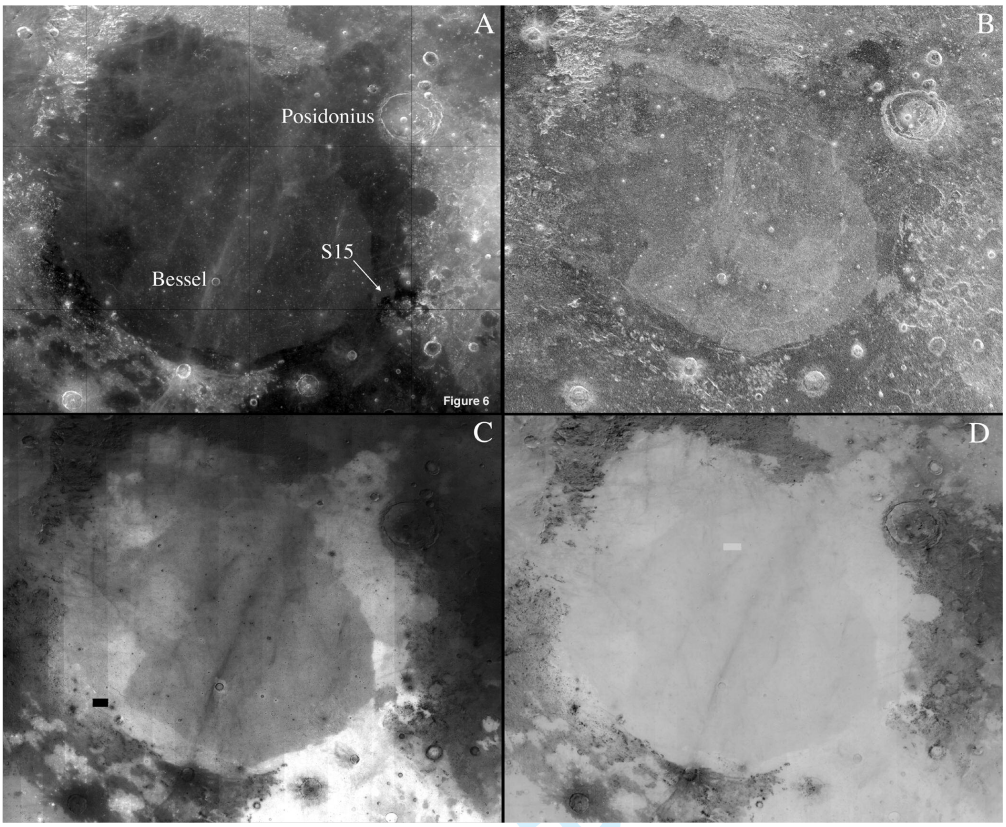

Figure 6

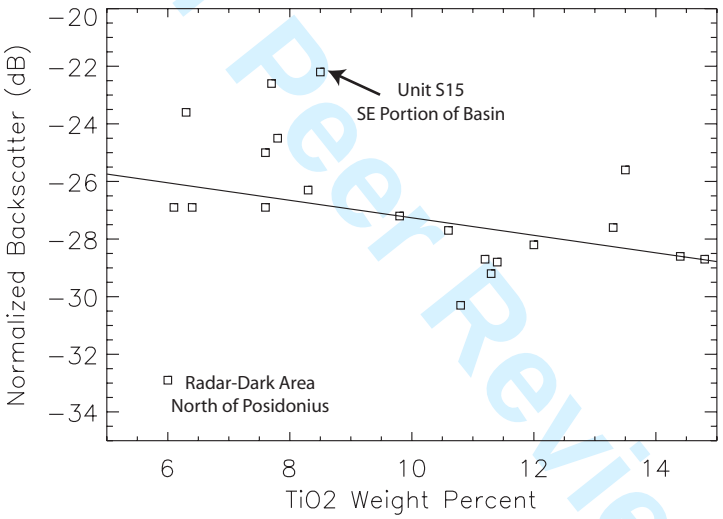

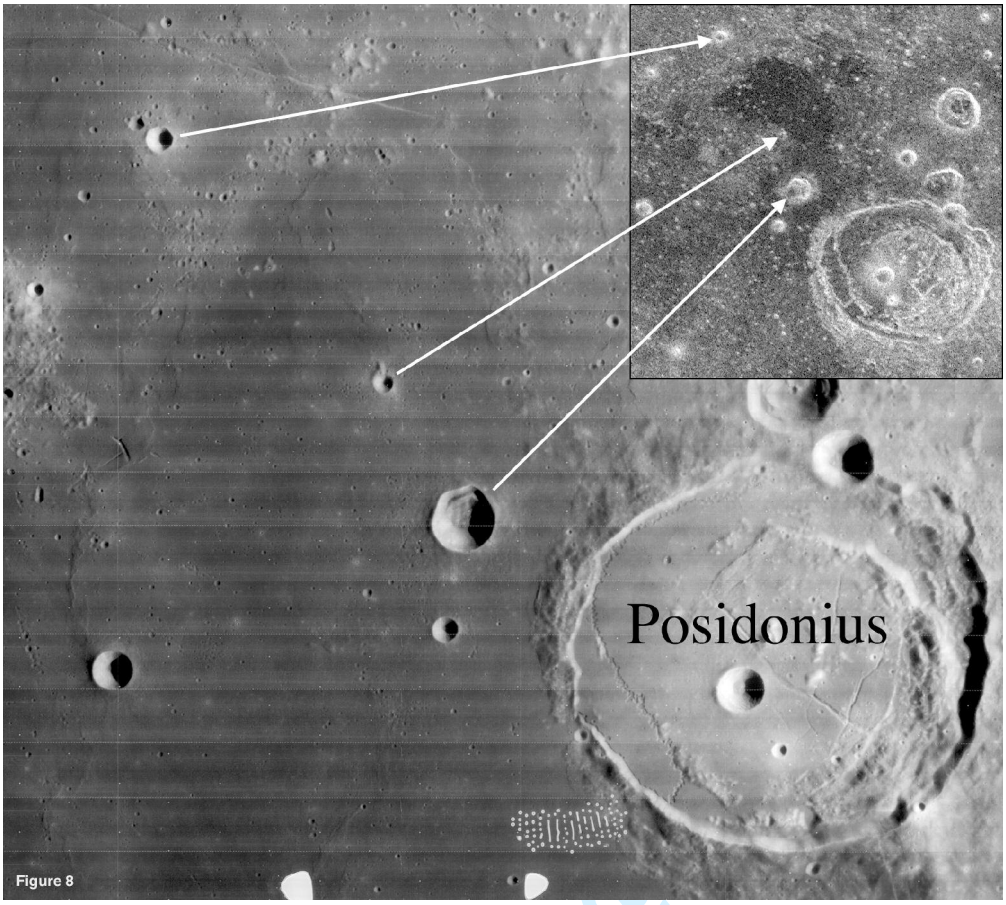

Figure 8